Decadal Variability in Coupled Sea-Ice–Thermohaline Circulation Systems*

JIAYAN YANG

Department of Physical Oceanography, Woods Hole Oceanographic Institution, Woods Hole, Massachusetts

J. DAVID NEELIN

Department of Atmospheric Sciences and Institute of Geophysics and Planetary Physics, University of California, Los Angeles, Los Angeles, California

(Manuscript received 27 September 1996, in final form 10 March 1997)

ABSTRACT

An interdecadal oscillation in a coupled ocean–ice system was identified in a previous study. This paper extends that study to further examine the stability of the oscillation and the sensitivity of its frequency to various parameters and forcing fields. Three models are used: (i) an analytical box model; (ii) a two-dimensional model for the ocean thermohaline circulation (THC) coupled to a thermodynamic ice model, as in the authors' previous study; (iii) a three-dimensional ocean general circulation model (OGCM) coupled to a similar ice model. The box model is used to elucidate the essential feedbacks that give rise to this oscillation and to identify the most important parameters and processes that determine the period. Numerical experiments in the 2D THC–ice model show that the model stability is sensitive to the ocean–ice coupling coefficient, the eddy diffusivity, and the strength of the thermohaline-circulation feedback per unit surface-polar density perturbation. The coupled model becomes more stable toward low coupling, greater diffusion, and weaker THC feedback. The period of the oscillation is less sensitive to these parameters. Nonlinear effects in the sea-ice model become important in the higher ocean–ice coupling regime where the effective sea-ice damping associated with this nonlinearity stabilizes the model. Surface Newtonian damping is also tested. The 3D OGCM, which includes both wind stress and buoyancy forcings, is used to test this coupled ocean–ice mechanism in a more realistic model setting. This model generates an interdecadal oscillation whose characteristics and phase relations among the model variables are similar to the oscillation obtained in the 2D models. The major difference is that the oscillation frequency is considerably lower. This difference can be explained in terms of the analytical box model solution in which the period of the oscillation depends on the rate of anomalous density production by melting/cooling of sea ice per SST anomaly, times the rate of warming/cooling by anomalous THC heat advection per change in density anomaly. The 3D model has a smaller THC response to high-latitude density perturbations than in the 2D model, and anomalous velocities in the 3D case tend to follow the mean isotherms so the anomalous heat advection is reduced. This slows the ocean–ice feedback process, leading to the longer oscillation period.

1. Introduction

Interdecadal variations of oceanic temperature and salinity, and sea-ice extent in the North Atlantic Ocean are major signals in the marine climate system (Dickson et al. 1988; Mysak et al. 1990; Walsh and Chapman 1990). Notable variations include the Great Salinity Anomaly (GSA) in the North Atlantic Ocean in the 1970s (Mysak et al. 1990; Dickson et al. 1988). Recent analyses also reveal apparent quasi-oscillatory modes with interdecadal timescales in the North Atlantic (Kushnir 1994; Deser and Blackmon 1993) and globally (Ghil and Vautard 1991). Numerical models have suggested potential mechanisms for decadal oscillations associated with the thermohaline circulation (THC) (e.g., Weaver et al. 1991; Winton and Sarachik 1993; Delworth et al. 1993; Huang 1993, 1994; Chen and Ghil 1995). Such climate variations may result from interactions among different components of the climate system. Since the THC involves long timescales, it is potentially a rich source for such low-frequency variations. The THC variability is primarily controlled by those physical processes that determine the sea surface temperature (SST) and salinity (SSS) at the subpolar North Atlantic Ocean where deep water is formed. The presence of sea ice not only changes the surface heat flux but also modifies the surface freshwater flux. Sea ice is thus postulated to play an important role in the THC-related climate variations. The objective of this paper

---

* Woods Hole Oceanographic Institution Contribution Number 9409.

Corresponding author address: Dr. Jiayan Yang, Dept. of Physical Oceanography, Woods Hole Oceanographic Institution, Woods Hole, MA 02543.
E-mail: yang@seminole.whoi.edu

© 1997 American Meteorological Society

is to explore important feedbacks in the THC–sea-ice coupled system by using a hierarchy of models.

In a previous study, we suggested that a mechanism that involves active ocean–ice interaction may contribute to such variability (Yang and Neelin 1993, hereafter YN93). This paper extends the study of YN93 to examine this oscillation over a broad range of parameters and forcing fields, and to test it in a more realistic three-dimensional primitive equation model. This paper also presents an analytical solution to elucidate the essential physics of the oscillation. The effect of nonlinearity of the sea-ice model will also be discussed.

In the next section, models used in this study, including a two-dimensional THC model, a three-dimensional ocean general circulation model, and a thermodynamic sea-ice model, will be introduced. The solution of an analytical box model will be studied in section 3 to highlight the essential feedbacks that give rise to this type of oscillation. The sensitivity of this model to various physical parameters and forcings will be discussed in section 4 by using the same two-dimensional model as that in YN93. Results from the three-dimensional model will be discussed in section 5.

2. Models

a. A two-dimensional THC model

The zonally averaged THC model of YN93 is used to calculate the oceanic temperature, salinity, and velocity. The overturning circulation is driven by the meridional density gradient, that is,

$$A_V \frac{\partial^4 \psi}{\partial z^4} + A_H \frac{\partial^4 \psi}{\partial y^2 \partial z^2} = \frac{g}{\rho_0} \frac{\partial \rho}{\partial y}, \tag{1}$$

where ψ is the streamfunction; A_V and A_H are the vertical and horizontal eddy viscosities, respectively; ρ is the water density; and g is the gravitational acceleration rate.

The temperature and salinity are determined by advection and mixing:

$$\frac{\partial T}{\partial t} + \frac{\partial (vT)}{\partial y} + \frac{\partial (wT)}{\partial z} = \kappa_H \frac{\partial^2 T}{\partial y^2} + \kappa_V \frac{\partial^2 T}{\partial z^2} \tag{2}$$

$$\frac{\partial S}{\partial t} + \frac{\partial (vS)}{\partial y} + \frac{\partial (wS)}{\partial z} = \kappa_H \frac{\partial^2 S}{\partial y^2} + \kappa_V \frac{\partial^2 S}{\partial z^2}, \tag{3}$$

where κ_H and κ_V are horizontal and vertical diffusion coefficients. The model domain extends from 70°S to 70°N with a constant depth of 4000 m. The model resolution is 2° in the horizontal and 200 m in the vertical. Equations (1)–(3) are solved numerically, using boundary conditions of no-normal flow and no-normal flux at all rigid walls. No wind stress is applied at the surface. The so-called mixed boundary condition is used at the surface, in which the SST is dampened toward a prescribed equilibrium state while a virtual salt flux is applied to approximate the freshwater flux:

$$\rho C_p \kappa_V \frac{\partial T}{\partial z} = \begin{cases} \kappa_{aw}(T_e - T) & \text{if } \delta = 0 \\ \kappa_{iw}(T_f - T) & \text{if } \delta > 0 \end{cases} \tag{4}$$

$$\kappa_V \frac{\partial S}{\partial z} = \left(F(y) + \frac{\partial \delta}{\partial t} \right) S_0, \tag{5}$$

where T_e is a prescribed equilibrium temperature for the air–sea heat flux, which decreases sinusoidally from 27°C at the equator to the seawater freezing temperature $T_f = -2°\text{C}$ at the ice edge; κ_{aw} is the air–sea heat flux coefficient; and κ_{iw} is the water–ice heat flux coefficient, which is usually smaller than κ_{aw}; $F(y)$ is specified as an approximation to the evaporation-minus-precipitation rate; δ is the ice thickness; and S_0 is the mean surface salinity.

YN93 used a linear equation of state, that is, $\rho = \rho_0(1 - \alpha T + \beta S)$ with $\alpha = 2 \times 10^{-4}$ °C^{-1} and $\beta = 8 \times 10^{-4}$ psu^{-1}. The real equation of state is highly nonlinear in temperature. For example, the United Nations Educational, Scientific, and Cultural Organization (UNESCO) equation of state (Gill 1982) estimates that $\partial\rho/\partial T$ varies from -0.3 kg °C^{-1} at 25°C to -0.026 kg °C^{-1} at $-2°$ for S = 35 psu. Therefore, we include a nonlinear equation of state in this study. Following Winton and Sarachik (1993) we use a third-order polynomial approximation to the UNESCO equation:

$$\rho(T, S) = 0.7968S - 0.0559T - 0.0063T^2 + 3.7315 \times 10^{-5} T^3. \tag{6}$$

One of the most noticeable differences in using (6), as opposed to the linear equation in YN93, is that the overall THC strength is considerably weaker under the same forcing. The overturning cell is dominated by the thermal mode, and thus its strength is controlled to a large extent by the meridional density contrast contributed by temperature gradient. The use of (6) greatly reduces that temperature contribution to ρ in cold water. We adjust the values of A_V and A_H such that the model produces about 15 sverdrups (10^6 m^3 s^{-1}) of deep water.

Like many other THC models, the ocean model (1)–(3) with boundary conditions (4) and (5) produces multiple equilibria under hemispherically symmetric forcings. The symmetric two-cell circulation is unstable to finite-amplitude perturbations and can be shifted to a more stable one-cell circulation, such as Fig. 1 shown in YN93, with sinking near the northern boundary and upwelling elsewhere.

b. The three-dimensional model

The three-dimensional ocean model used in this study is the Geophysical Fluid Dynamics Laboratory (GFDL) Modular Ocean Model (MOM) (Pacanowski et al. 1993). The model physics, as described by Bryan (1969), uses the hydrostatic and Boussinesq approximations and a nonlinear equation of state. The numerical schemes are discussed in detail in Pacanowski et al.

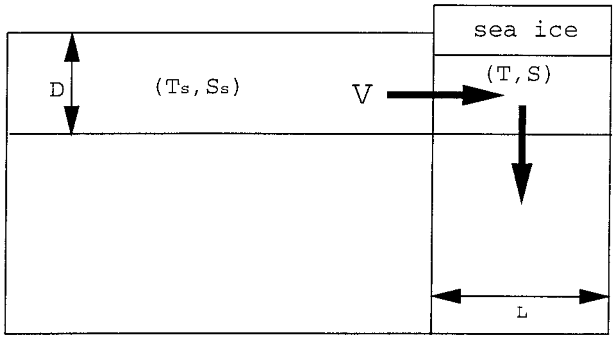

FIG. 1. Schematic of the box model.

(1993). In our application, a mixed boundary condition is used, in which the SST is relaxed toward the zonally averaged SST climatology of Levitus (1982), and the virtual salt flux is diagnosed from a steady state obtained by restoring the SSS to Levitus's salinity climatology. The model domain extends from 10° to 75°N. As we will discuss later in section 4, the coupled ocean–ice oscillation arising from using a half-basin model is quite similar to that using a full-basin model. Thus, the results from this half-basin model can be extended to a larger domain. Because long simulations are needed for each run, we decided to use a rather coarse resolution of 4° × 4° in the horizontal. A vertical depth of 4500 m is divided into 15 levels in thickness increments from 30 m at the surface to 630 m at the bottom. The relaxation time for the surface heat flux is 30 days.

c. A thermodynamic sea-ice model

The sea-ice model used in this study is the same as that used by Yang and Neelin (1996) and Zhang et al. (1995). This model, originally constructed by Welander (1977), is similar to that of Maykut and Untersteiner (1971). YN93 used this model to derive the linearized ice model used there. The detailed derivation can be found in these previous papers. Here we present only a brief description of how changes in the heat budget lead to freezing and melting.

Major heat fluxes at the upper surface of sea ice include solar radiation (F_{r}); longwave radiation from the atmosphere (F_{L}); reflected solar radiation (aF_{r}), where a is the surface albedo; outgoing radiation ($\varepsilon_{\mathrm{L}}\sigma T_{\mathrm{s}}^4$), where ε_{L} is the longwave emissivity, σ is the Stefan–Boltzmann constant, and T_s is the surface temperature of sea ice; and heat conduction $[-K_i(dT/dz)_{z=0}]$, where K_i is the thermal conductivity. In addition, there are several smaller fluxes, such as sensible heat flux (F_s), latent heat flux (F_l), and the penetrating radiative flux through the surface (I_0). Since the seasonal cycle is excluded in our model, we assume that the upper surface temperature of sea ice is always below the freezing point and no melting occurs at the upper surface. As discussed in Maykut and Untersteiner (1971) and in Thorndike (1992), a balance of the major heat fluxes at the upper surface takes the form

$$(1 - \alpha)F_{\mathrm{T}} - I_0 + F_{\mathrm{L}} - \varepsilon_{\mathrm{L}}\sigma T_{\mathrm{s}}^4 + K_i\left(\frac{dT}{dz}\right)_{z=0} = 0. \quad (7)$$

We now linearize the longwave radiation from the ice surface at the freezing temperature T_f, that is,

$$\varepsilon_{\mathrm{L}}\sigma T_{\mathrm{s}}^4 \approx \varepsilon_{\mathrm{L}}\sigma T_f^4 + (4\varepsilon_{\mathrm{L}}\sigma T_f^3)(T_{\mathrm{s}} - T_f), \quad (8)$$

and substitute it into (7):

$$K_i\left(\frac{dT}{dz}\right)_{z=0} = \kappa_{ai}(T_a - T_{\mathrm{s}}), \quad (9)$$

where $\kappa_{ai} = 4\varepsilon_{\mathrm{L}}\sigma T_f^3$ and $T_a = (1 - a)F_r - I_0 + F_{\mathrm{L}} + 3\varepsilon_{\mathrm{L}}\sigma T_f^4/\kappa_{ai}$, with T_a the equilibrium temperature for the surface heat flux that would be the sea-ice surface temperature if there were not upward heat conduction, and κ_{ai} the surface heat flux coefficient. Thorndike (1992) estimated that the value for κ_{ai} is about 4.6 W m^{-2} °C^{-1} for $\varepsilon_{\mathrm{L}} = 1$, $\sigma = 5.7 \times 10^{-8}$ J m^{-2} s^{-1} K^{-4}, and $T_f = 271.2$ K. In this paper we will use $\kappa_{ai} = 5.0$ W m^{-2} °C^{-1}.

At the bottom of the sea ice, the growth rate of sea ice is determined by the difference of upward heat conduction and heat flux from the ocean F_w, that is,

$$\rho_i L_f \frac{\partial \delta}{\partial t} = K_i\left(\frac{dT}{dz}\right)_{z=-\delta} - F_w, \quad (10)$$

where ρ_i is the density of sea ice and L_f is the latent heat of fusion.

We further assume that the sea-ice temperature profile is linear in the vertical, with uniform upward heat conduction:

$$K_i\left(\frac{dT}{dz}\right)_{z=-\delta} = K_i\left(\frac{dT}{dz}\right)_{z=0} = \frac{K_i(T_{\mathrm{s}} - T_f)}{\delta}. \quad (11)$$

The heat flux from ocean to sea ice, F_w, is poorly estimated. A linear Newtonian relaxation form is often used in which F_w is related to the difference between the freezing temperature that applies in a thin boundary layer at the ice's lower surface, and the ocean temperature $T|_{z=0}$ below this layer:

$$F_w(T) = \kappa_{iw}(T - T_f), \quad (12)$$

where κ_{iw} is the water–ice heat flux coefficient. Note that T is the ocean temperature for the surface layer just below an assumed thin wall layer at the water–ice interface where the temperature transitions to the freezing temperature, T_f. The water–ice heat exchange coefficient, κ_{iw}, characterizes the bulk exchange across this layer, just as κ_{aw} characterizes the exchange in open ocean regions according to (4). There is considerable variation in the value and interpretation of κ_{iw} in the literature. For instance, Houssais and Hibler (1993) take the ocean temperature immediately below the ice to be at freezing. Although this would appear similar to specifiying a large value of κ_{iw} in (12), it in fact assumes that the ocean model can resolve the thin transition layer. Under finite differencing, this is equivalent to having κ_{iw} set by the ocean surface diffusivity and resolution. Our usage assumes a bulk parameterization for the wall layer and is consistent with Willmott and Mysak (1989). The heat diffusion into the thin mixed layer is estimated to be $\rho C_p \kappa_V (T - T_f)/\Delta z$, where C_p is the specific heat of seawater and κ_V is the vertical diffusivity. For $\Delta z = 200$ m, $\rho = 1000$ kg m^{-3}, and $C_p = 4000$ J kg^{-1}, the heat flux coefficient $\kappa_{iw} = \rho C_p \kappa_V/\Delta z$ ranges from 1 to 10 W m^{-2} °C^{-1} for κ_V varying from 0.5×10^{-4} m^2 s^{-1} to 5×10^{-4} m^2 s^{-1}. This is considerably smaller than κ_{aw}, which is determined by linearizing the total air–sea heat flux (Haney 1971). In an equilibrium state, all heat that enters into the thin mixed layer beneath the sea ice must be diffused through the ice. If sea ice has an insulating effect, then κ_{iw} must be less than κ_{aw}.

Combining (10)–(12) yields the one-layer thermodynamic sea-ice model

$$\rho_i L_f \frac{\partial \delta}{\partial t} = \frac{\kappa_{ai} K_i (T_f - T_a)}{K_i + \delta \kappa_{ai}} - \kappa_{iw}(T|_{z=0} - T_f). \quad (13)$$

The coupling between the ocean and sea ice is through the surface freshwater flux term in the upper boundary condition (4) for the salinity and the water–ice heat flux term in (13).

The linearized version of this thermodynamic sea-ice model used in YN93 was

$$\frac{\partial \delta'}{\partial t} = -\frac{\kappa_{iw}}{\rho_i L_f} T' - \frac{\varepsilon_{iw}}{\rho_i L_f} \delta', \quad (14)$$

where δ' and T' are anomalous ice thickness and SST, respectively, and $\epsilon_i = \kappa_{iw}/\rho_i L_f$ is an effective damping coefficient resulting from the dependence of heat conduction on ice thickness. When sea ice is thicker, the heat flux from ocean to atmosphere through the upward heat conduction inside sea ice becomes less efficient, and therefore, ice tends to melt at the water–ice interface. This process provides a restoring of sea ice toward an equilibrium thickness δ_0. The damping coefficient, determined by linearization of the nonlinear sea-ice model about the equilibrium state, is given by

$$\epsilon_i = \frac{K_i \kappa_{ai}^2 (T_f - T_a)}{(K_i + \kappa_{ai}\delta_0)^2 \rho_i L_f}. \quad (15)$$

Within the reasonable range of parameters, ϵ_i varies from (5 yr)$^{-1}$ to (15 yr)$^{-1}$.

Coupling the THC model to the nonlinear sea-ice model with freely varying ice edge will be discussed in section 4f. The linearized version will be used for most runs of the two-dimensional model and for the analytical box model. Coupling of the nonlinear ice model to the OGCM is discussed in section 5.

3. Sea-ice–THC interaction on interdecadal time scales—A box model

A remaining important issue regarding the YN93 sea-ice–THC oscillation mechanism is what sets the period of the oscillation. The primary purpose of this section is to elucidate such parameter dependences by using a box model. Such a box model has proven useful in a recent study on feedbacks of sea ice on the THC stability in response to long-term climatic forcings (Yang and Neelin 1996). This model consists of four boxes, two in the upper layer to represent the high- and low-latitude surface regions, respectively, and another two to divide the deep ocean (Fig. 1). The THC variations of interest are localized near the deep convection region in YN93. Furthermore, they occur as variations about a state that always has a mean poleward flow at the surface and polar sinking. Using upstream differencing between the boxes, variations in the deep polar box do not affect the surface polar box. If we neglect variations in the low-latitude boxes relative to the surface polar box, the surface polar T, S equations decouple from the other boxes. This reduction is not suitable for THC multiple equilibria, but it captures the essential oscillation mechanism of interest here. The linearized equations for surface polar temperature and salinity anomalies, determined by the advection and the surface fluxes, are

$$\frac{\partial T'}{\partial t} + \frac{V_0}{L} T' - \frac{\Delta T_0}{L} v' + \frac{\kappa_{iw}}{\rho C_p D} T' = 0 \quad (16)$$

$$\frac{\partial S'}{\partial t} + \frac{V_0}{L} S' - \frac{\Delta S_0}{L} v' - \frac{S_0}{D} \frac{\partial \delta'}{\partial t} = 0, \quad (17)$$

where V_0 and v' are the mean and the anomalous meridional velocities, respectively; ΔT_0 and ΔS_0 the differences of the mean surface temperature and salinity between the low- and high-latitude boxes; L and D are the meridional extent and the depth of the surface polar box; and κ_{iw} is the heat flux coefficient between sea ice and the ocean.

For the temperature equation (16), the main contribution to the temperature change comes from the surface damping and the anomalous heat transport. The contribution of mean flow, which is usually smaller than other terms, acts as a damping, and its effect can be combined into the surface Newtonian cooling term. Like most box models, the meridional velocities are proportional to the density differences between the two surface boxes, that is,

$$v' = \gamma(-\alpha T' + \beta S'). \quad (18)$$

Due to a strong surface damping on SST, the first term on the right-hand side of (18) is small, and it only contributes a small additional damping to SST when (18) is substituted into (16). Therefore, we may assume that the anomalous circulation is driven by the anomalous salinity alone. This simplification is strongly supported by the numerical model of YN93. The salinity change is totally dominated by the freshwater flux associated with the ice freezing and melting. The small damping effect of the mean flow is negligible, and the anomalous salinity advection is small since the mean gradient of salinity is quite small. As such, (16)–(18) can be simplified to

$$\frac{\partial T'}{\partial t} - \frac{\Delta T_0}{L}v' + \frac{\kappa_{iw}}{\rho C_p D}T' = 0 \tag{19}$$

$$\frac{\partial S'}{\partial t} - \frac{S_0}{D}\frac{\partial \delta'}{\partial t} = 0. \tag{20}$$

$$v' = \gamma\beta S'. \tag{21}$$

The linearized thermodynamic sea-ice model (14) is used here. At decadal timescales, the anomalous sea-ice growth rate is approximately determined by the anomalous heat flux from the ocean, that is, the first term on the rhs of (14). For simplicity, we can drop the second term on the rhs of (14). The eigenvalue of (18)–(21), plus (14) with this approximation, for time dependence exp(ωt), is

$$\omega = -\underbrace{\frac{\kappa_{iw}}{2\rho C_p D}}_{R_4} \pm i\left[\underbrace{\gamma\beta}_{R_1}\,\underbrace{\frac{\Delta T_0}{L}}_{R_2}\,\underbrace{\frac{S_0\kappa_{iw}}{D\rho_i L_f}}_{R_3} - \underbrace{\left(\frac{\kappa_{iw}}{2\rho C_p D}\right)^2}_{R_4}\right]^{1/2}. \tag{22}$$

As (22) shows, the frequency is not determined by any one oceanic or ice process alone, but rather by a combination of parameters from both, namely the circulation change per unit salinity change (R_1), the mean meridional temperature gradient leading to rate of SST change by anomalous advection (R_2), and the rate of freshening by ice melt per SST anomaly (R_3). The square root of the product of these gives the essence of the frequency. A modification to this frequency, plus a damping effect, is provided by the strength of surface damping on SST (R_4). Unfortunately, (22) does not provide an explanation for the growth of the oscillation in the more complex models, only for the period. Using the fuller box model equations (16)–(17), and the full ice equation (14), yields additional small damping terms, plus one term from ($-\Delta S_0 v'/L$) that tends to oppose damping but is too small to explain growth.

The interdecadal period is very robust in (22). For example, Fig. 2 shows the period $2\pi/\mathrm{Im}(\omega)$ as a function of κ_{iw} (the main tunable parameter in this box model) for the following values of parameters: $\Delta S_0 = 2$ psu, $\Delta T_0 = 15$°C, L = 1000 km, D = 1000 m, $S_0 = 35$ psu, $\alpha = 1.5 \times 10^{-4}$ C^{-1}, $\beta = 8 \times 10^{-4}$ psu^{-1}; $\gamma = DV_0/(-\alpha\Delta T_0 + \beta\Delta S_0)$ is chosen such that the mean deep water formation rate DV_0 is 15 Sv. As Fig. 2 shows, the period approaches infinity when the coupling coefficient κ_{iw} approaches 0 (approaching the uncoupled regime). As κ_{iw} increases, the feedback process accelerates and the period of the oscillation shortens. Except for a small parameter regime for weak coupling, the period of the oscillation is at interdecadal timescales between 10 and 15 yr.

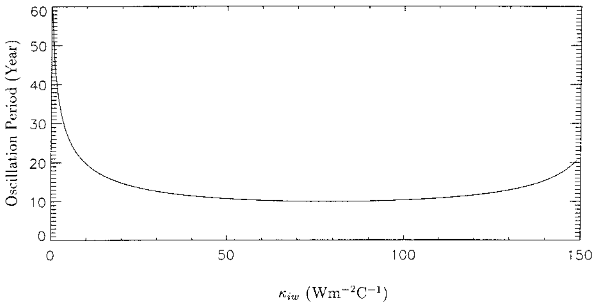

FIG. 2. The oscillation period as a function of ice–water coupling coefficient as determined by a solution [(22)] to the analytical box model.

4. Ocean–ice interaction and interdecadal oscillations in the two-dimensional model

The analytical solution presented in the previous section suggests that the oscillation and its frequency are dependent on various parameters and processes, such as the water–ice heat flux coefficient κ_{iw}, which controls both sea-ice growth rate and the damping by surface fluxes on SST variation in the ice-covered areas, the dynamical response of the circulation to the density change, eddy diffusivity, and the freshwater flux associated with sea-ice melting/freezing, etc. We investigate sensitivity to such parameters in the two-dimensional ice–THC model in this section.

a. Sensitivity to the coupling coefficient κ_{iw}

The most important parameter in this system is probably the water–ice heat flux coefficient κ_{iw}. The coupling between the THC and sea ice is essentially through the heat flux between water and ice, which in turn controls the temporal change of sea-ice thickness. This heat flux plays both stabilizing and destabilizing roles. A stronger heat flux coefficient results in greater Newtonian damping on the SST variation in the ice-covered area, providing a negative feedback to the system. The development of the coupled oscillation, however, relies on the same heat flux coupling, as measured by this coefficient, to melt ice.

The model produces oscillations in almost the entire range of κ_{iw}, although it is stable at the low coupling limit. The values of other physical parameters chosen in this section are $\kappa_{\mathrm{V}} = 5 \times 10^{-5}$ m^2 s^{-1}, $\kappa_{\mathrm{H}} = 1 \times 10^2$ m^2 s^{-1}, $\epsilon_i = (15\ \mathrm{yr})^{-1}$, while $A_{\mathrm{V}} = 60$ m^2 s^{-1} and $A_{\mathrm{H}} = 6 \times 10^7$ m^2 s^{-1} are chosen such that the THC transport is 15 Sv for a basin width of 6000 km. The

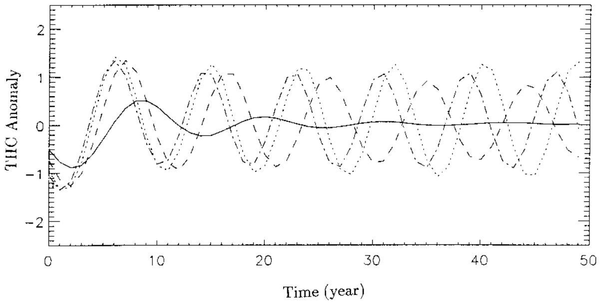

FIG. 3. Time series of anomalous THC overturning strength, defined as the maximum anomalous streamfunction times a zonal width of 6000 km, in the 2D coupled ocean–ice model between 66° and 70°N at 1000 m in depth for κ_{iw} = 1 W m^{-2} °C^{-1} (solid line), 15 W m^{-2} C^{-1} (dashed line), 50 W m^{-2} °C^{-1} (dotted line), and 150 W m^{-2} °C^{-1} (dashed–dotted line). Unit: Sv (10^{6} m^{3} s^{-1}).

value of κ_{aw} is chosen to give a 1-yr relaxation timescale for SST, $\kappa_{aw}/(\rho C_p D) = (1/\text{yr})^{-1}$, in the upper 200 m; $F(y)$ is diagnosed from a steady state, which is achieved by strongly constraining the SSS toward the Levitus (1982) climatology; S_0 = 35 psu; $T_f = -2$°C is the freezing temperature.

Figure 3 shows a 50-yr time series of anomalous THC overturning for various values of κ_{iw}. The anomalous THC is defined in this 2D model as the maximum anomalous streamfunction times a zonal width of 6000 km. The solid line is in the very low coupling regime, κ_{iw} = 1 W m^{-2} °C^{-1}. At such weak coupling, the model is stable and produces a damped oscillation with a period of about 12 yr. As discussed in the next section, the oscillation can be sustained by stochastic forcing. In the moderate coupling regime (κ_{iw} = 15 W m^{-2} °C^{-1}; dashed line), the oscillation is self-sustaining with a period of about 10 yr. If we further increase the coupling to κ_{iw} = 50 W m^{-2} °C^{-1}, the period is shortened to about 9 yr (dotted line). At a very strong coupling (κ_{iw} = 150 W m^{-2} °C^{-1}), the period is shortened to about 8.2 yr (the dashed–dotted line). This agrees with our analytical solution (22), which suggests that the period is longer at weaker coupling. The period is fairly insensitive to this coupling coefficient since it only changes from 12 to 8.2 yr as coupling is changed by more than two orders of magnitude. The reasons for this small sensitivity can be understood by reference to the box model (22). There are two terms in (22) that can affect the oscillation frequency ω. First, the main oscillation term—the product $R_1 R_2 R_3$—depends on κ_{iw} via R_3, the freshwater feedback from sea-ice. Second, R_4 from damping on SST variations also has a κ_{iw} dependence. A greater κ_{iw} accelerates the ocean–ice feedback loop and tends to shorten the oscillation period (R_3). It also dampens T', increasing R_4, and thus tends to slow the feedback. These two effects cancel each other to a certain extent and reduce the overall sensitivity of ω in (22) to κ_{iw}. The amplitude of THC variation is about 1 Sv for most cases except the very small coupling case (κ_{iw} = 1 W m^{-2} °C^{-1}). The anomalous SSS and ice thickness in these cases vary around 0.1 psu and 0.25 m. The anomalous SST varies from about 0.25°C at low coupling to less than 0.05°C at high coupling.

The critical value of κ_{iw} for sustained oscillation is about 15 W m^{-2} °C^{-1} for the chosen parameter values. As we shall see later, this critical coupling coefficient becomes smaller for smaller diffusivities. For instance, Fig. 4 shows the anomalous THC for κ_{iw} varying from 5 to 15 W m^{-2} °C^{-1} when κ_V and κ_H are reduced to 1 × 10^{-5} and 1 × 10^{6} m^{2} s^{-1}, respectively. The oscillation can be sustained at about κ_{iw} = 12 W m^{-2} °C^{-1} for this smaller diffusion regime.

The intrinsic physics of the oscillation is explained by the feedback loop of YN93. For example, Fig. 5 shows four model variables at 67°N for κ_{iw} = 25 W m^{-2} °C^{-1}. The anomalous circulation (solid line) is driven by the salinity anomaly (dashed line), and therefore the former lags the latter by about a quarter cycle. The salinity rate of change is dictated by the sea-ice rate of change (dashed–dotted line) and so they are almost in phase. The sea ice is controlled by the SST anomaly (dotted line). As shown in YN93, the surface salinity anomaly (Fig. 6b) is strongly localized in the area of sea-ice variation (Fig. 6d). The temperature (Fig. 6a) and circulation (Fig. 6c) vary over broader areas.

b. *Stochastic forcing in a weak coupling regime*

In the previous section, we discussed the model sensitivity to the coupling coefficient κ_{iw}. We found that the oscillation period is fairly insensitive to this parameter, but the model is stable at a lower coupling regime. In this section, we will show that even without instability at this regime, the oscillation can be forced by random noise. In the real climate system both the ocean and the atmosphere are constantly subject to different temporal- and spatial-scale forcings. There has been increasing interest in the role of stochastic forcing in generating low frequency climate variability. Hasselmann (1976) noted that the heat capacity of the upper ocean can act as an integrator for random heat fluxes from the atmosphere and yield a red noise response. Mikolajewicz and Maier-Reimer (1990) applied stochastic forcings to an OGCM and found significant model variability on interdecadal to centennial timescales. Attempts have been made to explain such variability in terms of Hasselmann's stochastic model. But it remains unclear what determines the intrinsic frequencies, if any, in ocean models. In our model, we know that a clear decadal period is determined by the THC–sea-ice feedback. We are interested in the effect of stochastic forcing on this oscillation when it is stable. For the same parameter setting as in section 4a, Fig. 7 displays two examples of stochastically forced runs. In these two cases, a temporally white but spatially correlated noise is applied to the equilibrium temperature for heat flux for a particular latitude band. The spatial dependence is a half-sinusoidal curve from 60° to 70°N with an amplitude of 2°C.

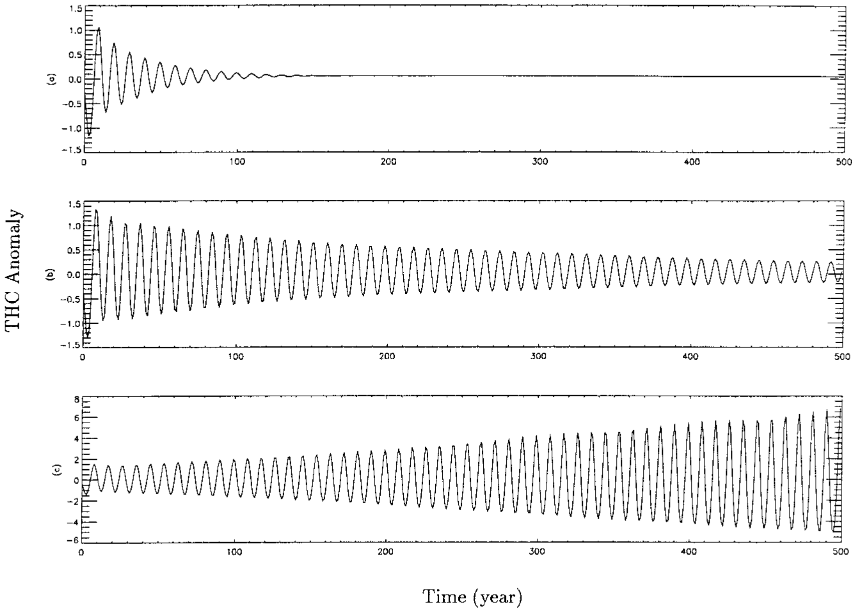

FIG. 4. Time series of anomalous THC strength (Sv; defined as in Fig. 3) in the weak diffusion regime of the 2D model at $\kappa_V = 1 \times 10^{-5}$ m^2 s^{-1} for (a) weak coupling at $\kappa_{iw} = 5$ W m^{-2} °C^{-1}, (b) moderate coupling at $\kappa_{iw} = 10$ W m^{-2} °C^{-1}, and (c) stronger coupling at $\kappa_{iw} = 15$ W m^{-2} °C^{-1}.

This is multiplied by a random variable from a uniform distribution. For $\kappa_{iw} = 1$ W m^{-2} °C^{-1} (Fig. 7a), the unforced coupled model produces a damped oscillation (solid line) while the oscillation is sustained by the random forcing. Figure 7b shows the case when the same stochastic forcing is applied to the model at $\kappa_{iw} = 5$ W m^{-2} °C^{-1}. The amplitude of the noise-forced oscillation increases with coupling since the decay rate is smaller. In both cases, the decadal timescale can be clearly seen despite the aperiodicity introduced by noise. In an uncoupled run, no decadal period is found and the amplitude of the response is much smaller (Fig. 8). Without the sea-ice feedback, the SST (Fig. 8a) varies without a clearly defined frequency, a typical result for a system that integrates the white random forcings to yield a red spectrum response (Hasselmann 1976). Since the salinity is no longer connected with temperature variations via sea ice, its response is very small (Fig. 8b), which leads to a very weak response in the THC as well (Fig. 8c).

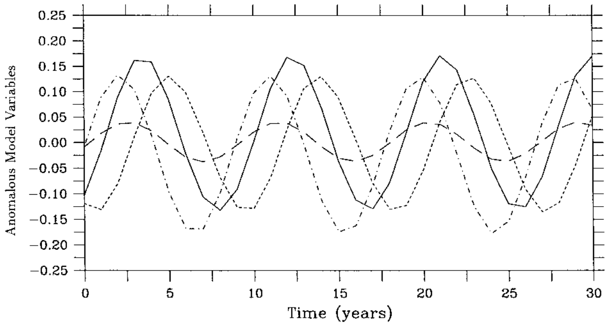

FIG. 5. A 30-yr segment for anomalies of streamfunction (solid), temperature (dotted), salinity (dashed), and ice thickness (dashed–dotted) taken at the surface at 67°N near the northern boundary of the 2D model. Units: m^2 s^{-1} for streamfunction, °C for temperature, psu for salinity, and m for ice thickness.

c. Sensitivity to the eddy diffusivity

Parameter settings are as in section 4a, with stronger coupling $\kappa_{iw} = 25$ W m^{-2} °C^{-1}. Here we vary the diffusivity κ_V of both salinity and temperature, while changing the lateral diffusivity κ_H proportionately. Figure 9a shows the anomalous THC overturning for $\kappa_V = 1 \times 10^{-4}$ m^2 s^{-1}. With this high diffusivity, the oscillation is slowly decaying (Fig. 9a), although essentially with the same period and characteristics discussed for the case with lower diffusivity and coupling in section 4a. As the diffusivity is reduced, for $\kappa_V = 5 \times 10^{-5}$ m^2 s^{-1}, instability of this oscillation gives rise to a limit cycle solution to the coupled system (Fig. 9b). As the diffusivity is decreased to $\kappa_V = 1 \times 10^{-5}$ m^2 s^{-1}, a second bifurcation occurs and the model generates both the decadal oscillation and longer timescale variations. In this case, the amplitude of the decadal oscillation slowly increases with time until the excursions become comparable to the magnitude of the mean overturning. Eventually, the reduced overturning phase shuts down the circulation to the point where it can no longer sustain the decadal oscillation, which then builds up again from low amplitude. This behavior is very similar to that of

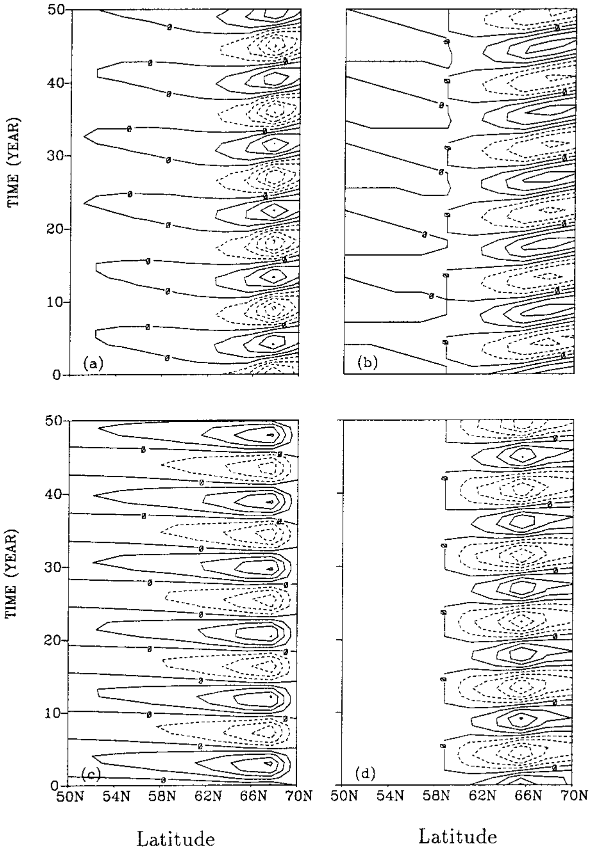

FIG. 6. Latitude–time plots for anomalies of (a) temperature, (b) salinity, (c) streamfunction, and (d) sea-ice thickness. Contour intervals: 0.05°C, 0.025 psu, 0.05 $m^2 s^{-1}$, and 0.05 m.

the Rossler attractor (e.g., Nayfeh and Balachandran 1995; Strogatz 1994), which fundamentally involves three directions in the phase space: a spiral out from an unstable stationary point and reinjection into the vicinity of this point by nonlinear terms, via a third direction. The resulting motions may be chaotic. While this behavior is very interesting, it is not clear whether it is relevant to the observed ocean–ice system. An overall conclusion is that although the variation of the eddy diffusivity changes the model stability, the period of the decadal oscillation remains essentially unchanged.

d. Model sensitivity to the THC feedback

One crucial part of the feedback loop is the THC change per density change. In the box model, the period has roughly a square root dependence on this parameter. In the 2D model, this is harder to directly control with the available physical parameters. As a test, we introduce a control parameter μ such that

$$\psi(y, z, t) = \psi_0(y, z) + \mu\psi'(y, z, t), \qquad (23)$$

where ψ is the total streamfunction, ψ_0 is the mean streamfunction from the THC climatology, and ψ' is the deviation of ψ from its mean and is driven by the density anomaly according to the momentum equation (1). By varying the parameter μ, we can change the THC response to a density anomaly without altering the mean field. Based on a limited number of runs (not shown), the period indeed appears to roughly follow a $\mu^{1/2}$ dependence. When μ increases, it accelerates the feedback loop linking the surface freshwater flux to the THC heat transport and therefore shortens the period of the oscillation, supporting the analytical result (22).

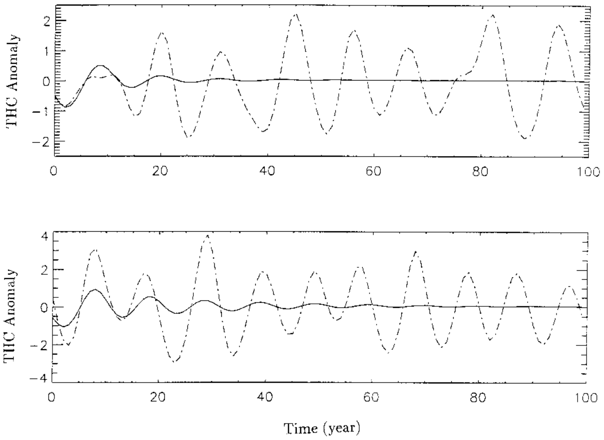

FIG. 7. Anomalous THC strength (as in Fig. 3) in the weak coupling regime of the 2D model, (a) for $\kappa_{iw} = 1$ W m^{-2} °C^{-1} and (b) for $\kappa_{iw} = 5$ W m^{-2} °C^{-1}. In both panels, the dashed–dotted line shows a run with stochastic forcing, while the solid line shows a run evolving without stochastic forcing from an initial anomaly.

e. Newtonian damping on the SST variation

The Newtonian relaxation form for the surface heat flux provides an effective damping on the SST variation

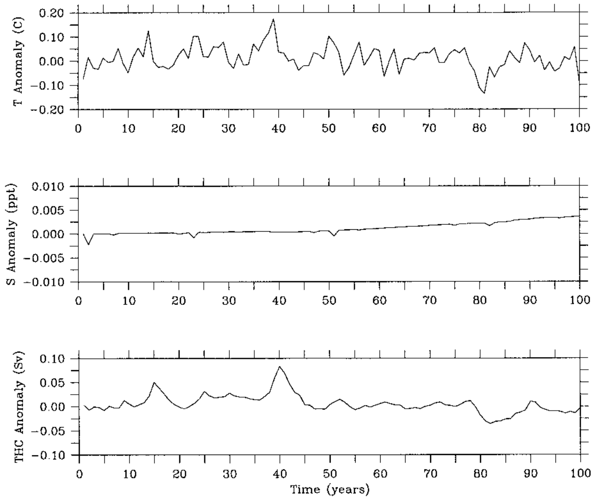

FIG. 8. Anomalies of (a) temperature (°C), (b) salinity (psu), and (c) THC overturning strength (Sv) of the 2D ocean-only model with stochastic forcing.

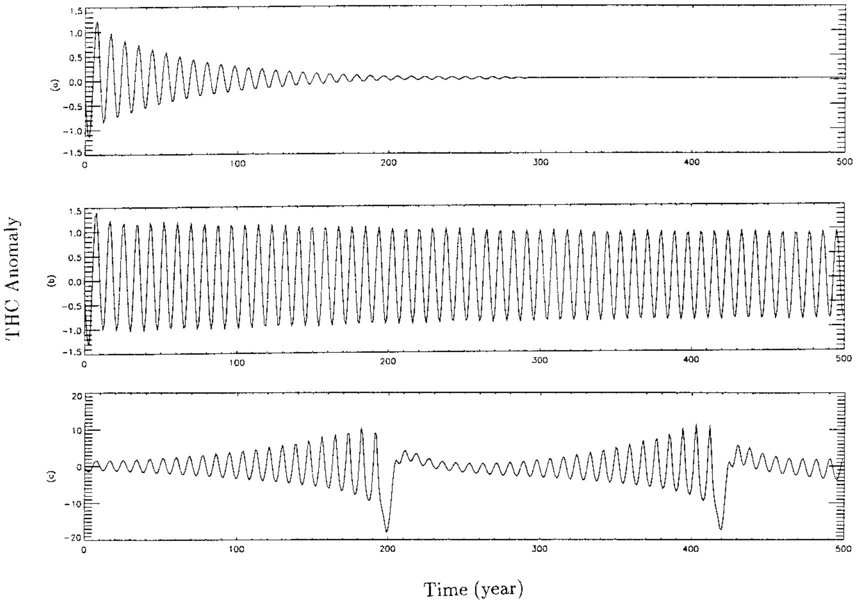

FIG. 9. Time series of anomalous THC strength (as in Fig. 3) for different diffusivities: (a) strong diffusion, (b) moderate diffusion, and (c) weak diffusion. Unit: Sv.

and provides a negative feedback to the decadal oscillation. To examine the impact of this on the oscillation without change of the model climatology, we modify the damping on the anomalous SST only. A control parameter ν is introduced so that the surface condition (5) can be written as

$$\rho C_p \kappa_V \frac{\partial T}{\partial z} = \kappa_{iw}(T_f - \overline{T}) - \nu \kappa_{iw} T', \qquad (24)$$

where $\overline{T}$ is the mean SST. In this experiment, we also assume that the enhanced surface damping on the SST does not affect the ocean–ice coupling coefficient in the sea-ice equation [i.e., ν is only applied to (24)].

Parameter settings are as in section 4a, with $\kappa_{iw} = 25$ W m^{-2} °C^{-1}. For stronger damping at $\nu = 2$, the oscillation is stable. For $\nu = 1$ the oscillation is sustained as shown before. When ν is decreased to 0.5, a 19-yr period oscillation arises (Fig. 10) due to period doubling of the decadal oscillation. For even smaller damping, the model generates chaotic oscillations (not shown).

f. The nonlinearity of the sea-ice model

The nonlinearity of the sea-ice model comes from the heat conduction term, that is, the first term on the right-hand side of (13). In this section, we use the same THC model and couple it to the fully nonlinear ice model (13). At a steady state, the mean sea-ice thickness is determined

$$\overline{\delta} = \frac{K_i(T_f - T_a)}{\kappa_{iw}(T - T_f)} - \frac{K_i}{\kappa_{ai}}, \qquad (25)$$

by where $\overline{\delta}$ and $\overline{T}$ are the mean ice thickness and SST, respectively. For smaller κ_{iw}, the mean ice thickness $\overline{\delta}$ is greater. For thinner mean ice, the effective damping on sea-ice variability is greater according to (15).

Figure 11 shows the anomalous THC overturning for various values of the coupling coefficient κ_{iw}, with other parameters as in section 4a. For weak coupling at $\kappa_{iw} = 2.5$ W m^{-2} °C^{-1}, the oscillation is in the decaying regime in the nonlinear coupled model (Fig. 11a). For

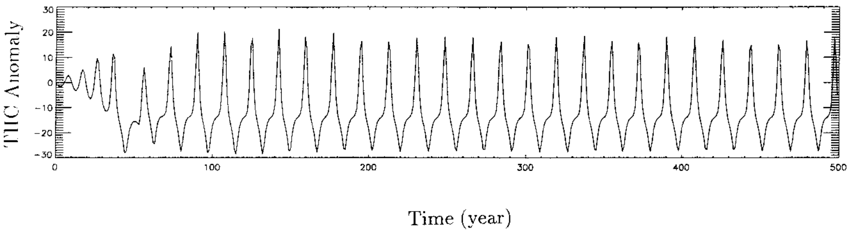

FIG. 10. Anomalous THC strength (as in Fig. 3) for a case with weaker Newtonian damping [$\nu = 0.5$ in (24)]. Unit: Sv.

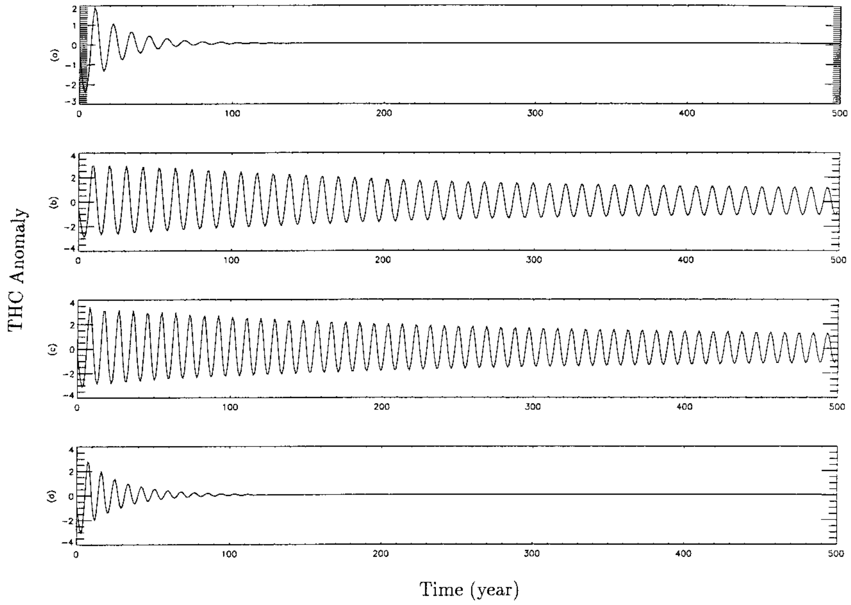

FIG. 11. Anomalous THC strength (as in Fig. 3) from coupling to the nonlinear version of the sea-ice model with freely varying ice edge (a) $\kappa_{iw} = 2.5$ W m^{-2} °C^{-1}; (b) $\kappa_{iw} = 5$ W m^{-2} °C^{-1}; (c) $\kappa_{iw} = 10$ W m^{-2} °C^{-1}; and (d) $\kappa_{iw} = 15$ W m^{-2} °C^{-1}.

greater coupling coefficient, $\kappa_{iw} = 5$ W m^{-2} °C^{-1} (Fig. 11b) and $\kappa_{iw} = 10$ W m^{-2} °C^{-1} (Fig. 11c), the oscillation slowly decays from its initial amplitude and equilibrates to an oscillation with smaller amplitude, about 0.5 and 0.6 Sv in these two cases, respectively. However, if κ_{iw} is further increased to 15 W m^{-2} °C^{-1}, the oscillation again decays relatively quickly. The period of the oscillation for these four different parameter values varies from 11 to 9 yr, with a longer period in the low coupling regime. Therefore, the nonlinearity does not significantly affect the frequency. The major change in comparing with cases that use the linearized sea-ice model is the loss of instability in the large coupling regime. This is because the ice thickness is very thin according to (25) when a greater κ_{iw} is used. For example, the average mean ice thickness ranges from 0.9 m at $\kappa_{iw} = 15$ W m^{-2} °C^{-1} to 2.5 m at $\kappa_{iw} = 5$ W m^{-2} °C^{-1}. For thicker sea ice, the effective damping is greater. This explains why the nonlinear sea-ice model does not have sustained oscillation in the high coupling regime.

Figure 12 shows a case for a weaker diffusion regime, $\kappa_V = 1 \times 10^{-5}$ m^2 s^{-1} for the same values of κ_{iw} as in Fig. 11. Again, the solution is stable for a weaker coupling (Fig. 12a for $\kappa_{iw} = 2.5$ W m^{-2} °C^{-1}). The oscillation grows initially before it reaches another stationary point for $\kappa_{iw} = 5$ W m^{-2} °C^{-1}. When κ_{iw} is further increased to 10 W m^{-2} °C^{-1}, the decadal oscillation is sustained with an amplitude of about 10 Sv (Fig. 12c), much greater than that in the stronger diffusion regime. The model is stable for an even greater κ_{iw} (Fig. 12d) for the same reason as explained above. Like the previous case, the frequency is fairly insensitive to the coupling coefficient κ_{iw}. Figure 13 shows snapshots of anomalous model conditions when the THC is at its peak for the case of $\kappa_{iw} = 10$ W m^{-2} °C^{-1}. The upper layer is warmer (Fig. 13a) due to poleward heat transport, which melts sea ice and results in lower surface salinity (Fig. 13b) and density (Fig. 13c). This is consistent with the physical explanation of YN93.

g. Equivalence of the interdecadal ice–THC oscillation in one-cell and two-cell cases

Most THC models, including the zonally averaged model used in this study, possess multiple equilibrium states for given parameters (Bryan 1986; Marotzke et al. 1988; Welander 1986). Like our previous study (YN93), most results have been presented for a decadal oscillation about a pole-to-pole one-cell THC climatology. In order to produce such an oscillation, the important property is that the THC responds positively (negatively) to a positive (negative) density anomaly at high latitudes. Therefore, the model is not sensitive to which THC is used as the model climatology as long as there is polar sinking and the model parameters are kept unchanged. The only noticeable difference is that the two-cell THC overturning is somewhat weaker in comparison with the one-cell state. Therefore, the damping associated with the mean flow on the temperature anomaly is smaller. When comparing results using these two climatologies, we found that the periods are essentially unchanged but the amplitude of the oscillation is greater for the two-cell case (not shown). This holds despite differences between the mean surface T–S fields in these two climatologies. The Northern Hemisphere is saltier and warmer in the one-cell case due to the

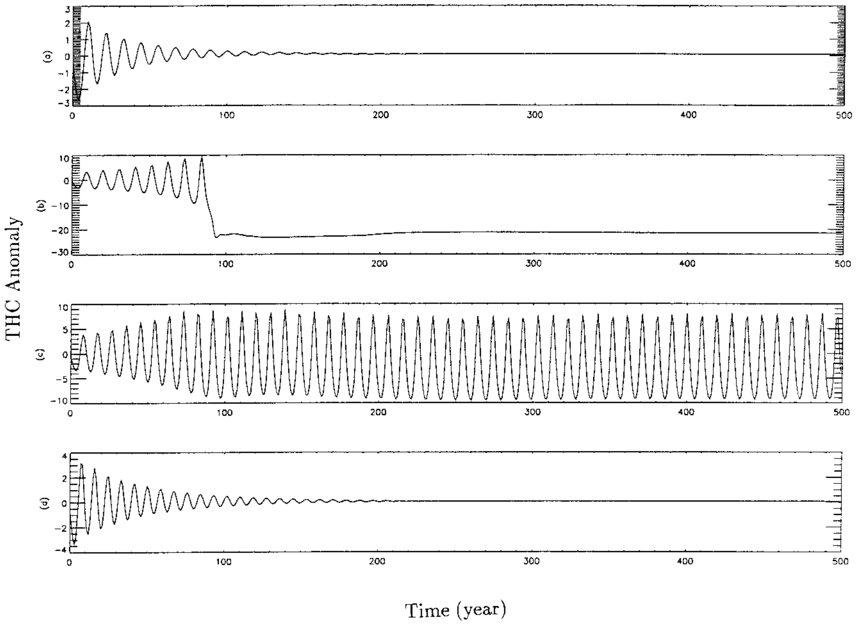

FIG. 12. As in Fig. 11 but with a smaller eddy diffusivity, $\kappa_V = 1 \times 10^{-5}$ m^2 s^{-1}.

across-equator transports. The change in the mean salinity has little effect on the oscillation since the salinity anomaly is dominated by sea-ice melting and freezing. The temperature gradient could potentially have a strong effect on the oscillation since it directly affects anomalous heat advection, but the difference in the mean $\partial T_0/\partial y$ between these two climatologies is small because of the strong Newtonian relaxation. In conclusion, the decadal oscillation remains virtually the same when a two-cell symmetric THC climatology is used.

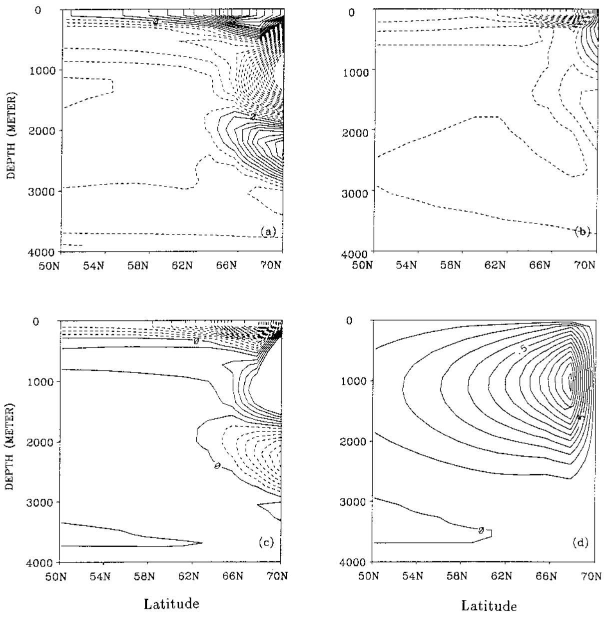

FIG. 13. Snapshot of the model condition at a time of peak circulation: (a) temperature anomaly (°C), (b) salinity anomaly (psu), (c) density anomaly (kg m^{-3}), and (d) anomalous THC strength (Sv; as in Fig. 3). Contour intervals: 0.01°C, 0.01 psu, 0.005 kg m^{-3}, and 0.1 Sv.

h. Use of a sponge layer in a smaller model domain

Although the two-dimensional ice–THC model is useful for diagnosing the physical mechanism, our ultimate goal is to study the ice–THC oscillation in a three dimensional OGCM. Such a task requires a tremendous amount of computing resources for the timescale of interest. As shown in that of YN93, the ice–THC oscillation is confined to a relatively small area in the vicinity of the sea ice. It should thus be possible to simulate it using a relatively small portion of the ocean basin, using a sponge layer to mimic an open-boundary condition. We test this in the two-dimensional model as an aid in preparing GCM experiments. In the sponge layer, the temperature and salinity are damped toward their climatological values. To make our point that a small ocean domain can be successfully used, we truncate the southern portion rather severely, placing the sponge layer at 50°N. The coupling coefficient is fixed at 25 W m^{-2} °C^{-1} and other parameters are as shown in section 4a and Fig. 5. Figure 14 shows the anomalous THC overturning strength for this sponge layer case (solid line) and a full-basin model (dashed line). The periods of their oscillations are exactly the same. The amplitude of the sponge layer is somewhat greater, perhaps due to increases in anomalous circulation per density anomaly in the severely truncated basin. These results suggest that it is very reasonable to use a regional North Atlantic OGCM with a sponge layer at the southern boundary to capture this oscillation.

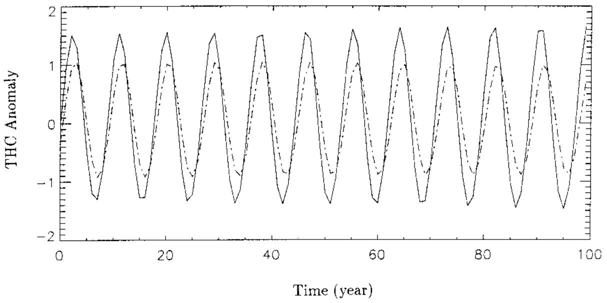

FIG. 14. Comparison of anomalous THC strength (as in Fig. 3) obtained from a full-basin 2D model solution (dashed–dotted line) to a solution from a model version with a sponge layer at 50°N model (solid line). Unit: Sv.

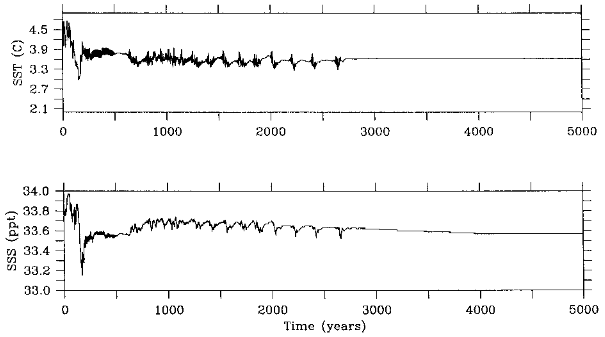

FIG. 15. Time series of the zonally averaged (a) SST and (b) SSS at 68°N over a 5000-yr spinup process in the 3D OGCM. Units: °C and psu.

5. Coupled ocean–ice oscillation in a three-dimensional model

In previous sections, the role of ocean–ice interaction in forcing a type of interdecadal oscillations is examined in simple models, including an analytical box model and a zonally averaged two-dimensional model. The mechanism of this oscillation needs to be tested in a primitive equation model before it can be extended to explain interdecadal oscillations either from a GCM simulation or from an observation. In this section, we present results from a coupled ocean–ice model that consists of the GFDL OGCM MOM and a nonlinear thermodynamic sea-ice model (13). The model domain, resolution, and forcing fields are described in section 2b. We first run the OGCM for 5000 yr to an approximately steady state and then diagnose the virtual salt flux from this state. The surface salinity condition is then switched from Newtonian restoring to flux form. The model is restarted and run for another 5000 yr to get the new quasi-steady state under the mixed boundary condition. To show this spinup process, we plot time evolution of the zonally averaged SST (Fig. 15a) and SSS (Fig. 15b) between 66°N and 70°N from the second 5000-yr run using the mixed boundary condition. The model fluctuates after switching to the new boundary condition but reaches a steady state after about 3000 yr. Figure 16 shows the zonally averaged distributions of (a) temperature and (b) salinity. The maximum temperature is about 25°C, located in the surface near the southern boundary. The maximum salinity occurs in the subtropics. The model does not include the seasonal cycle, and thus nonlinear subharmonic variations (e.g., Yang and Huang 1996; Yang and Honjo 1996) are excluded.

The active coupling with the sea-ice model (13) is turned on at the end of this second 5000-year run. We chose the equilibrium temperature (T_a) to vary sinusoidally from -5°C at 40°N to -35°C at the northern boundary and set $\kappa_{ai} = 5$ W m^{-2} °C^{-1}. This form of T_a is specified roughly according to the winter air temperature in the ice-covered region in the subpolar North Atlantic (Oort 1983). This produces a sea-ice cover north of 52°N for the standard run, using $\kappa_{iw} = 5$ W m^{-2} °C^{-1}. The model oscillates when ice interaction is included. Figure 17 shows a 1000-yr evolution of sea-ice thickness, SST, and SSS taken at 68°N in midbasin. The period of the oscillation is about 25 yr. The mechanism for this oscillation is essentially the same as that explained in the previous section. A careful examination shows that the sea-ice variation lags that of SST by one-quarter of a cycle, while the peak of sea-ice variation leads the trough of SSS variation by a quarter cycle. This phase relation is very similar to that found in the YN93's coupled ocean–ice oscillation. The overturning circulation also oscillates with the same frequency. Figure 18 shows the overturning cell at maximum and minimum strength during one oscillatory cycle. The THC varies from about 13 to about 7.5 Sv in this run. Because of this oscillation, the northward transport of heat also oscillates. The total northward transport of heat at 50°N

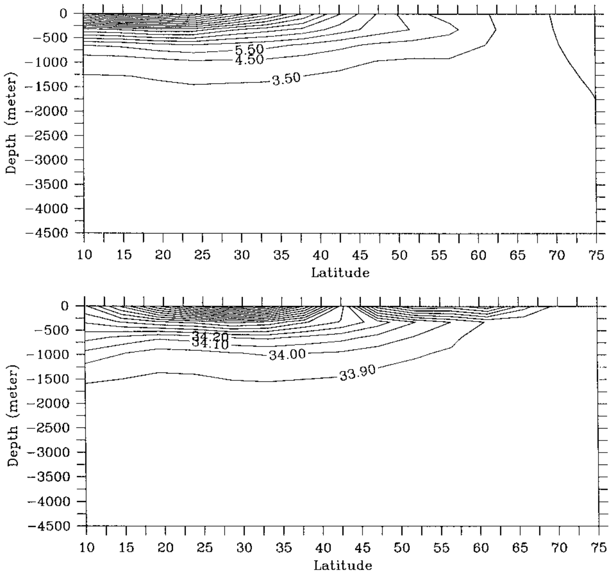

FIG. 16. The zonally averaged (a) temperature and (b) salinity at the equilibrium state of the 3D OGCM after the spinup run (contour intervals: 1°C and 0.1 psu).

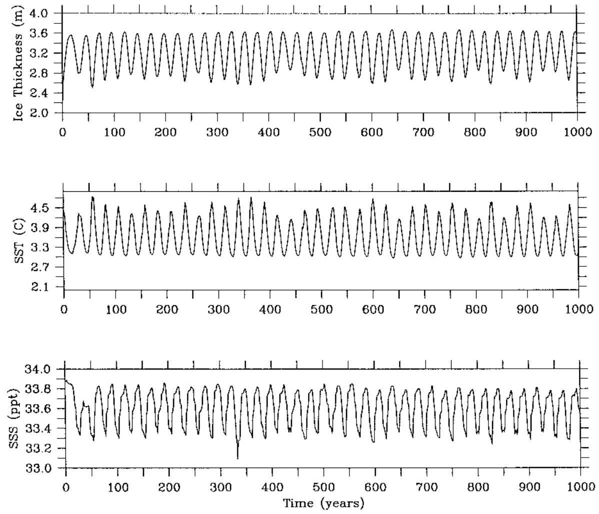

FIG. 17. Evolution over 1000 yr of (a) sea-ice thickness, (b) SST, and (c) SSS taken at 68°N in the center of the zonal domain from the 3D coupled OGCM–sea-ice model (κ_{iw} = 5 W m^{-2} °C^{-1}). Units: °C and psu.

oscillates between about 0.2 and 0.3 PW (Fig. 19). Figure 20 shows the maximum and minimum sea-ice distributions and the difference between these two phases. The ice edge slightly changes between these two states in the central and eastern parts of the basin, but the change of the ice edge per se is not the dominant feature of the differences. The change in ice thickness occurs over a broad region, especially in the central part of the domain and with amplitude near the ice edge of up to 1.1 m. Circulation in the wind-driven horizontal gyres exhibits relatively small change, as seen, for instance, in the depth-integrated transport streamfunction (Fig. 21).

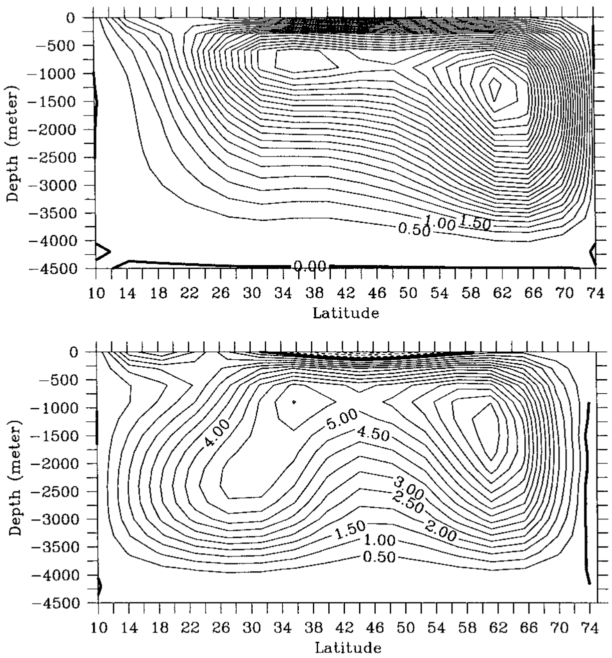

FIG. 18. Streamfunction for the zonally integrated transport form the 3D coupled model at the time of (a) the maximum and (b) the minimum strength of the overturning cell in the last oscillatory cycle before the end of the 1000-yr run shown in Fig. 7. Contour: 0.5 Sv.

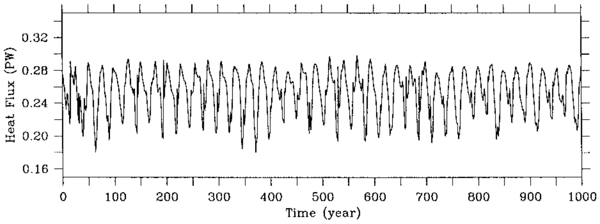

FIG. 19. Time series over 1000 yr from the 3D coupled model of the total northward transport of heat at 50°N. Unit: PW.

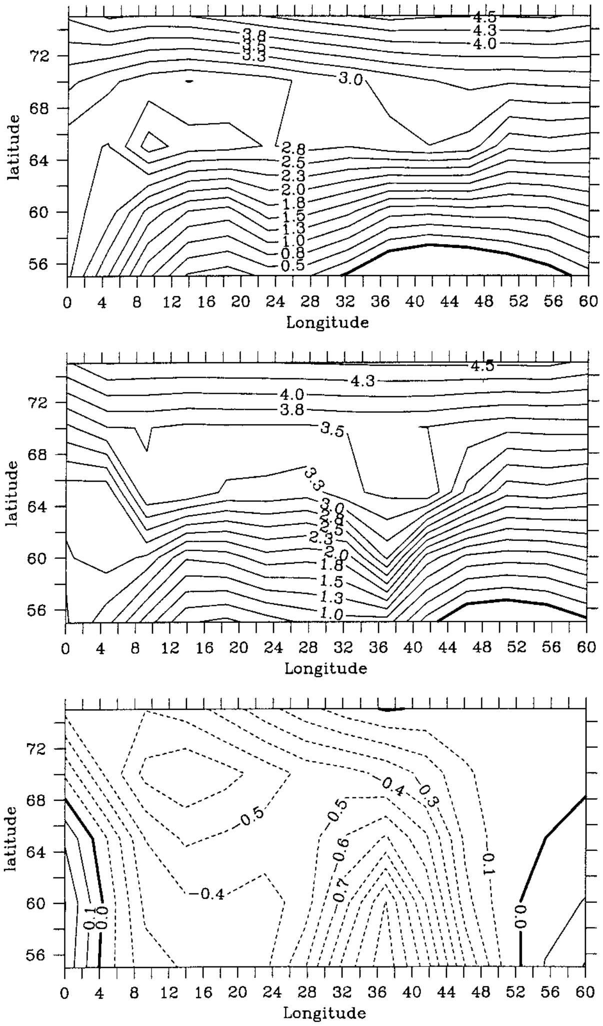

FIG. 20. Distribution of sea-ice thickness over the northern part of the domain of the 3D coupled model at times of (a) the minimum and (b) the maximum sea-ice and areal coverage, and (c) the difference between these two states. Contour interval: 0.25 m. Zero line is thickened.

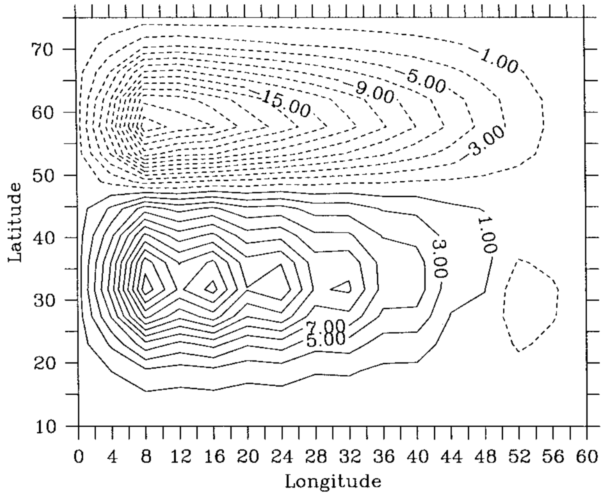

FIG. 21. The barotropic transport streamfunction in the 3D model. Unit: Sv.

The anomalous temperature distributions at warm (Fig. 22a) and cold (Fig. 22b) phases show that the maximum variations occur in the upper 1000 m over a region about 20° latitude wide near the northern boundary. The salinity variations (Fig. 23) are likewise trapped in the upper 1000 m. They are more localized near the northern boundary in the ice region during fresh or salty phases. During transition phases, additional salinity anomalies due to advection may be noted south of the ice region.

The oscillation characteristics are consistent with the YN93 results. It is worth underlining that this oscillation is not the same as the heat–ice oscillation identified by Welander (1977) and recently examined by Zhang et al. (1995) in a 3D model. The heat–ice oscillation discussed in those two papers arises due to change of sea-ice extent and the associated change in thermal insulation effect and salinity does not play a significant role. Welander's (1977) model did not include salinity and a similar freshwater conceptual model was used by Zhang et al. (1995) to explain their model oscillations. In contrast, salinity plays a leading role in our model oscillation. Turning off the salinity feedback from sea-ice melting and freezing stabilizes the model state and the oscillation disappears. In addition, the heat–ice oscillation of Welander (1977) and Zhang et al. (1995) should become more robust when a smaller ocean–ice heat flux coefficient κ_{iw} is used since it amplifies the effect of thermal insulation. As shown in the following sensitivity test, oscillations are damped when a smaller κ_{iw} is used in our model.

Figures 24 and 25 show the sensitivity to the ocean–ice coupling coefficient, κ_{iw}. When the value of this parameter is reduced from 5 to 2 W m^{-2} °C^{-1}, the model becomes stable and no oscillation is generated (Fig. 24). The model produces chaotic variations when κ_{iw} is increased to 30 W m^{-2} °C^{-1} (Fig. 25). These are qualitatively consistent with the two-dimensional model's results shown in section 4a. Additional experiments also show that the model stabilizes in a more diffusive regime.

The most significant difference between the oscillation in the two dimensional model and the oscillation in the three-dimensional model is that the period is considerably longer in the latter. Since the same sea-ice model is used in both 2D and 3D cases, the differences are due to the model representations of oceanic processes. As explained in the simple box model (22), the oscillation period is controlled by a number of processes, labeled R_1, R_2, R_3, and R_4. Both R_4, which measures the ocean–ice coupling and the surface Newtonian damping on SST in ice-covered areas, and R_3, which measures the freezing/melting rate in response to an SST anomaly, remain unchanged since the same ice model is used. The cause for the longer oscillation period in the 3D model is most likely due either to the difference in the circulation response to density anomalies, that is, R_1 in (22), or to the differences in anomalous heat advection [R_2 in (22)] when the flow has a three-dimensional structure. In the 3D case, the change of salinity, as shown in Fig. 17c, is about 0.5 psu, and the corresponding change of the THC is about 5.5 Sv (Fig. 18). However, in the 2D case, the surface salinity oscillates within 0.075 psu (dashed line in Fig. 5). The stream-

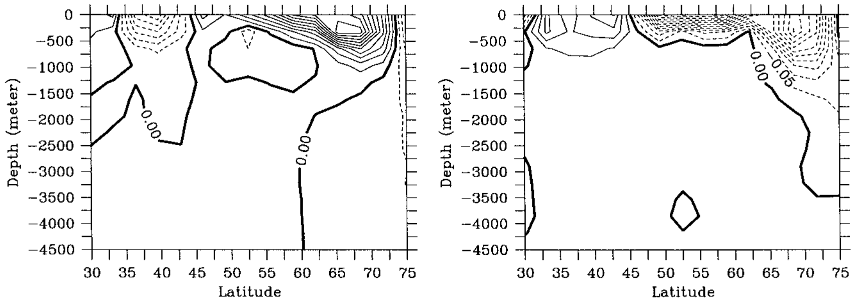

(a) Anomalous temperature

(b) Anomalous temperature

FIG. 22. Snapshots of anomalous zonally averaged temperature from the 3D model distribution at (a) a warm state and (b) a cold state. Both states were taken during the last oscillatory cycle before the end of the 1000-yr run shown in Fig. 7. Contour interval: 0.05°C.

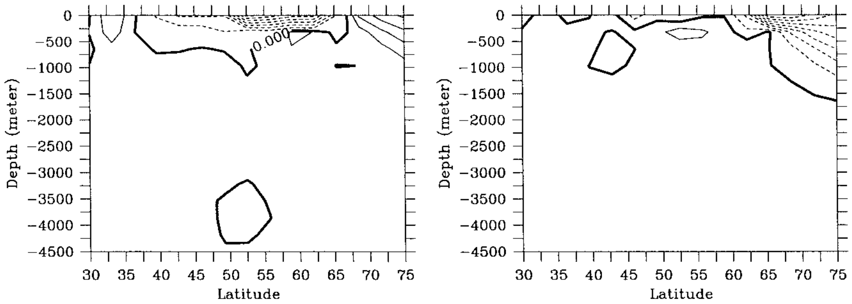

(a) Anomalous salinity (b) Anomalous salinity

FIG. 23. Snapshots of anomalous zonally averaged salinity from the 3D model taken at (a) a salty-to-fresh transitional phase, and at (b) a fresh phase. Both states were taken during the last oscillatory cycle before the end of the 1000-yr run shown in Fig. 7. Contour interval: 0.02 psu.

function anomalies in the same case varies between -0.125 m^2 s and 0.175 m^2 s, about -0.75 to 1.05 Sv for a basin width of 60° in longtitude. Therefore, the THC response per salinity anomaly, as measured by (21), that is, $\gamma\beta = v'/S'$, ranges from about 24 in the 2D case to about 11 in the 3D case. In other words, the THC has a greater response to the salinity anomaly in the 2D case than in the 3D case. Interpreted in terms of the box model solution, R_1 is smaller in the 3D model, which tends to lower the frequency of the oscillation. Considering the second possible cause associated with anomalous heat advection, in the 3D model, currents tend to have a large component along isotherms, whereas only the cross-isothermal component contributes to advection. The contour lines of temperature averaged over the upper 1000 m and the flow vectors in our 3D model clearly show this structure (Fig. 26). The upper branch of the overturning circulation is primarily along the western boundary where the isotherms are tilted northwestward in the same direction as the flow fields. Anomalous velocity, like the mean flow field, is greatest along the western boundary. For instance, Figs. 27a and 27b show the anomalous velocity (vectors) averaged in the upper 1000 m and anomalous upwelling (contours) at $z = -1000$ m in maximum and minimum states of the overturning circulation. Since the anomalous velocity, especially near the western boundary, tends to partially follow isotherms, the anomalous heat advection $\mathbf{v}'\boldsymbol{\nabla}T_0$ is correspondingly smaller than that in the 2D case, where isotherms are assumed zonal, resulting in larger advection for the same magnitude of overturning circulation anomaly. Interpreted in terms of the box model, R_2 in (22) is reduced in the 3D model, which tends to increase the oscillation period. The meridional temperature gradient averaged in the upper 1000 m, that is, $\int_{-D_0}^{0}(\partial T_0/\partial y)dz/D_0$ for $D_0 = 1000$ m, is about -2.5×10^{-5} cm^{-1} at 55°N in the 2D model and about -1.3×10^{-5} cm^{-1} in the western boundary layer of 20° in longitude, where the anomalous currents are strongest at the same latitude.

Fitting the roughly estimated numbers from these two processes into the box model solution (22), we find a period for the 3D oscillation of slightly more than twice that for parameters estimated from the 2D model. This agrees quite well with the actual model results. The smaller THC response to density changes and reduction of anomalous heat advection in the 3D model thus seems to explain the longer period of the coupled ocean–ice oscillations. The mechanism for the oscillation, however, is essentially the same as that explained in the box model solution (22) and in the two-dimensional model.

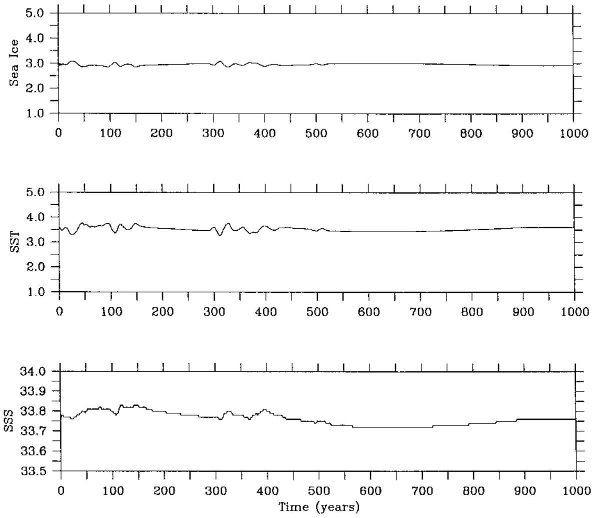

FIG. 24. As in Fig. 17 except using a smaller ocean–ice coupling coefficient ($\kappa_{iw} = 2$ W m^{-2} °C^{-1}).

6. Summary

In summary, we have reexamined the coupled ocean–ice oscillation previously identified by Yang and Neelin (1993), and tested its sensitivity to various physical parameters and surface forcing fields in a two-dimensional model and in a three-dimensional primitive equation model. An analytical box model is used to elucidate essential feedbacks that give rise to this oscillation and to identify the most important processes and parameters that determine the oscillation period. According to the

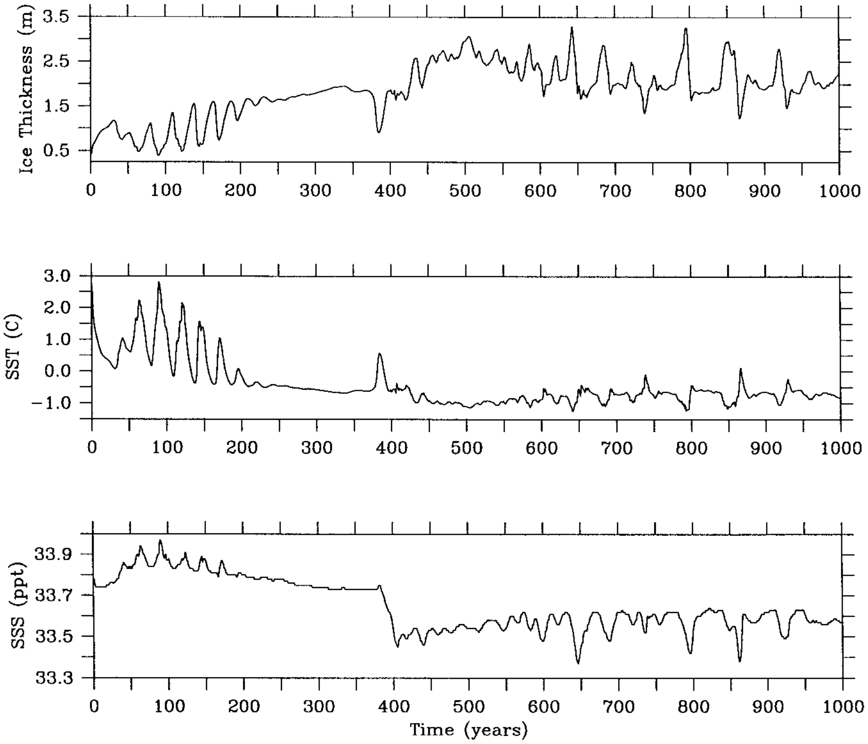

FIG. 25. As in Fig. 17 except using a greater ocean–ice coupling coefficient (κ_{iw} = 30 W m^{-2} °C^{-1}).

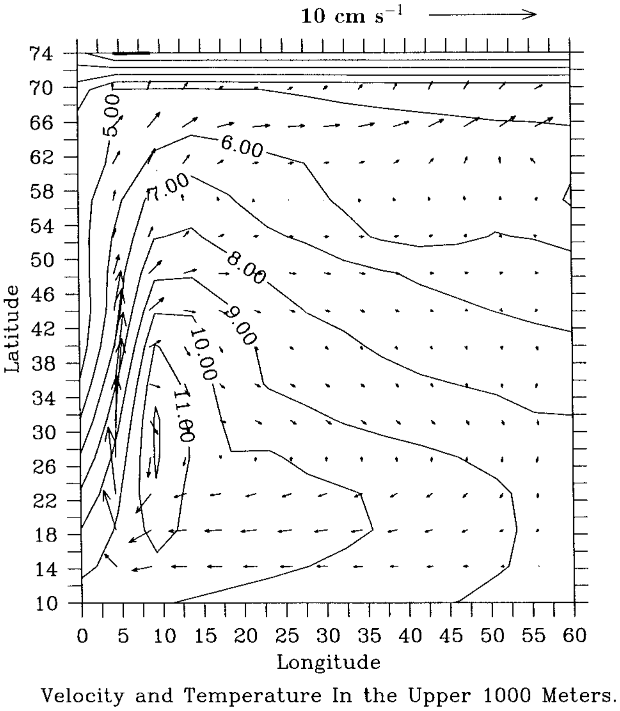

FIG. 26. Mean temperature contours and mean current fields (vectors) from the 3D model, both averaged in the upper 1000 m, for the case shown in Fig. 18.

box model, the oscillation mechanism can be summarized (dropping some quantitatively important but nonessential terms) by

$$\text{frequency} = [R_1R_2R_3]^{1/2},$$

where

R_1 = (THC velocity anomaly per salinity anomaly),

R_2 = (temperature gradient), and

R_3 = (rate of freshening by ice melt per SST anomaly).

A salinity increase in the sinking region causes an increase in the surface velocity of the overturning circulation (R_1; m s^{-1} psu^{-1}). This advects warm temperatures into the sinking region due to the temperature gradient between the sinking region and the region where the inflow comes from (R_2; K m^{-1}). The warming melts ice, which gives a freshening tendency that leads to the opposite phase of the cycle (R_3; psu s^{-1} K $^{-1}$). This makes clear that the oscillation timescale is truly a characteristic of the *coupled* system, depending on a combination of factors from both the ocean and the ice. None of these factors is a timescale characteristic of the individual systems.

When coupled with a linearized version of the sea-ice model, the 2D model becomes stable in the weak coupling regime and generates self-sustained oscillations as the ocean–ice coupling coefficient increases.

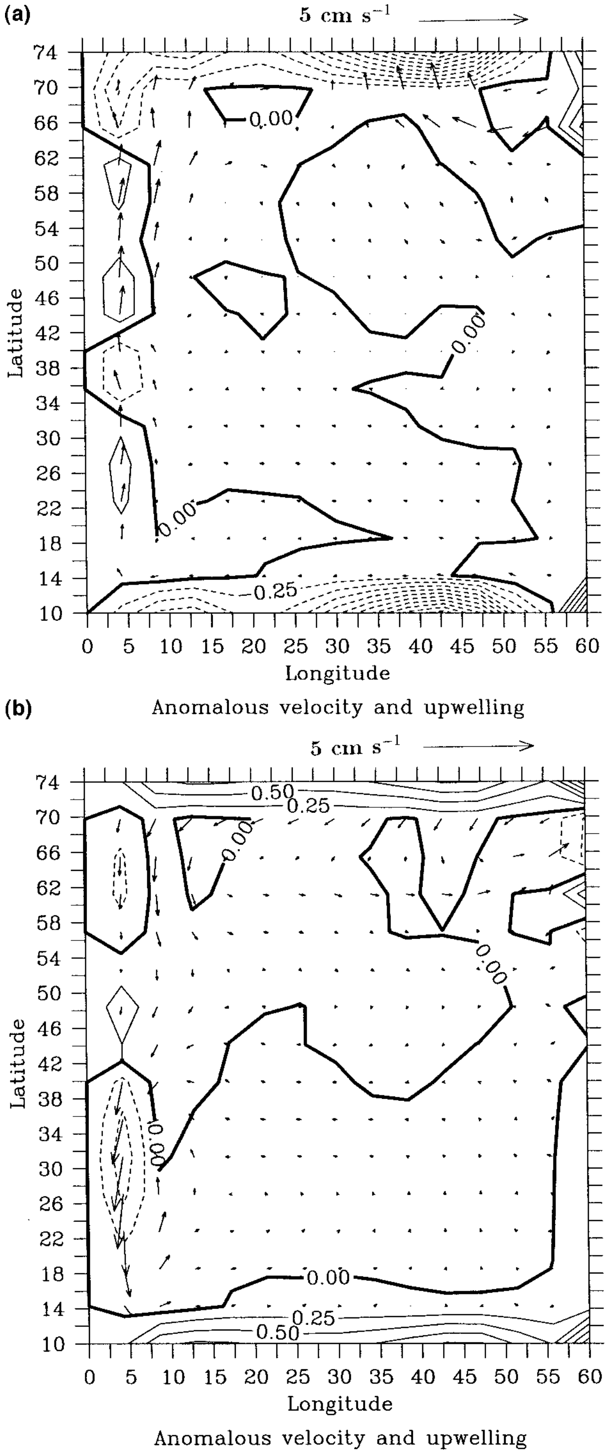

FIG. 27. Anomalous velocities (vector) averaged over the upper 1000 m and upwelling field (contour lines in m day^{-1}) at the depth of 1000 m (a) at a state of maximum THC overturning and (b) at a state of minimum THC overturning.

The oscillation period is quite insensitive to the intensity of this coupling. The model becomes more stable when greater diffusivity is used. In the stable parameter regime, interdecadal oscillations can be sustained by stochastic forcing. The coupled instability is sensitive to the amplitude of THC feedbacks, as determined by viscosities A_V and A_H in the 2D model equation (1) or γ in the box model solution (22). The model becomes more unstable and its oscillation period shortens toward greater THC feedback. We have also examined the case of using a nonlinear sea-ice model. The model behaves similarly as in the linear case when a small or an intermediate ocean–ice coupling coefficient is used, but becomes stable in high coupling regime. This can be explained in terms of the change of the effective damping on sea ice associated with the change of sea-ice thickness. The period of the oscillation in the nonlinear sea-ice case is also robust. Chaotic behavior of the oscillation was found in some parametric regimes. Insertion of a sponge layer in the 2D model is used to show that the essential variability is rather localized and thus a regional model can be used for studies with the 3D model. An additional experiment was run to show that the oscillation is also robust when a two-cell THC climatology is used.

Results from using the GFDL OGCM MOM coupled with the nonlinear sea-ice model are also presented. This 3D model also produces an interdecadal coupled ocean–ice oscillation. The mechanism is the same as that identified in the 2D model and explained in the box model. The major difference is that the period of oscillation becomes considerably longer, roughly 26 yr. The longer period is mainly due to a smaller THC response to salinity anomalies and to smaller poleward heat advection by anomalous flow fields in the 3D model compared to the 2D model. The box model explains the reduction in frequency as a reduction in both R_1 and R_2 (above). In terms of making a case for this oscillation mechanism being likely to occur in the observed ocean–ice system, some caveats on the 3D model are the lack of realistic geography, the relatively coarse resolution, the lack of ice advection, and the simple atmospheric boundary conditions. Nonetheless, the robustness of the oscillation in the two dimensional THC–ice model where it was first predicted, and the new demonstration of its existence in the three-dimensional model are encouraging. It suggests that this physical mechanism is worth seeking in data and in coupled ocean–atmosphere–ice GCMs.

Acknowledgments. This work was supported by NOAA Atlantic Climate Change Program Grant NA56GP0209 (JY), National Science Foundation Grants ATM-9158294 and ATM-9521389 (JDN and JY), a grant from the National Institute for Global Environmental Change (JDN and JY), and a Mellon Independent Study Award from the Woods Hole Oceanographic Institution (JY). We benefited from conversations with Drs. R. X. Huang, J. Marotzke, P. Stone, and J. Walsh. We thank Dr. A. Weaver and Mr. E. Wiebe for helpful comments, and welcome the news that this oscillation occurs in their ocean–atmosphere model (A. Weaver and E. Wiebe 1996, personal communication).

REFERENCES

Bryan, F. O., 1986: High-latitude salinity effects and interhemispheric thermohaline circulation. *Nature,* **323,** 301–304.

Bryan, K., 1969: A numerical method for the study of the circulation of the world ocean. *J. Comput. Phys.,* **4,** 347–376.

Chen, F., and M. Ghil, 1995: Interdecadal variability of the thermohaline circulation and high-latitude surface fluxes. *J. Phys. Oceanogr.,* **25,** 2547–2568.

Delworth, T., S. Manabe, and R. J. Stouffer, 1993: Interdecadal variations of the thermohaline circulation in a coupled ocean–atmosphere model. *J. Climate,* **6,** 1993–2011.

Deser, C., and M. L. Blackmon, 1993: Surface climate variations over the North Atlantic Ocean during winter: 1900–1989. *J. Climate,* **6,** 1743–1753.

Dickson, R. R., J. Meincke, S. A. Malmberg, and A. J. Lee, 1988: The ‘‘great salinity anomaly’’ in the northern North Atlantic 1968–1982. *Progress in Oceanography,* Vol. 20, Pergamon Press, 103–151.

Ghil, M., and R. Vautard, 1991: Interdecadal oscillations and the warming trend in global temperature time series. *Nature,* **350,** 324–327.

Gill, A. E., 1982: *Atmosphere–Ocean Dynamics.* Academic Press, 662 pp.

Haney, R. L., 1971: Surface thermal boundary conditions for ocean general circulation models. *J. Phys. Oceanogr.,* **1,** 241–248.

Hasselmann, K., 1976: Stochastic climate models. *Tellus,* **28,** 473–485.

Houssais, M. N., and W. D. Hibler III, 1993: Importance of convective mixing in seasonal ice margin simulations. *J. Geophys. Res.,* **98,** 16 427–16 448.

Huang, R. X., 1993: Real freshwater flux as a natural boundary condition for salinity balance and thermohaline circulation forced by evaporation and precipitation. *J. Phys. Oceanogr.,* **23,** 2428–2446.

——, 1994: Thermohaline circulation: Energetics and variability in a single hemisphere basin model. *J. Geophys. Res.,* **99,** 12 471–12 485.

Kushnir, Y., 1994: Interdecadal variations in North Atlantic sea surface temperature and associated atmospheric conditions. *J. Climate,* **7,** 141–157.

Levitus, S., 1982. Climatological atlas of the world ocean. NOAA Prof. Paper 13, U.S. Government Printing Office, Washington, DC, 173 pp. [Available from U.S. Government Printing Office, Washington, DC 20402.]

Marotzke, J., P. Welander, and J. Willebrand, 1988: Instability and multiple steady states in a meridional plane model of the thermohaline circulation. *Tellus,* **40A,** 162–172.

Maykut, G. A., and N. Untersteiner, 1971: Some results from a time-dependent, thermodynamic model of sea-ice. *J. Geophys. Res.,* **76,** 1550–1575.

Mikolajewicz, U., and E. Maier-Reimer, 1990: Internal secular variability in an ocean general circulation model. *Climate Dyn.,* **4,** 145–156.

Mysak, L. A., D. K. Manak, and R. F. Marsden, 1990: Sea-ice anomalies observed in the Greenland and Labrador Seas during 1901–1984 and their relation to an interdecadal Arctic climate cycle. *Climate Dyn.,* **5,** 111–133.

Nayfeh, A. H., and B. Balachandran, 1995: *Applied Nonlinear Dynamics, Analytical, Computational, and Experimental Methods.* John Wiley and Sons, 685 pp.

Oort, A., 1983: Global atmospheric circulation statistics 1958–1973. NOAA Prof. Paper 14, U.S. Government Printing Office, Washington, DC, 174 pp. [Available from U.S. Government Printing Office, Washington, DC 20402.]

Pacanowski, R. C., K. Dixon, and A. Rosati, 1993: The GFDL modular ocean model users guide. GFDL Ocean Group Tech. Rep., 232 pp. [Available from U.S. Government Printing Office, Washington, DC 20402.]

Strogatz, S. H., 1994: *Nonlinear Dynamics and Chaos.* Addison-Wesley Publishing, 498 pp.

Thorndike, A. S., 1992: A toy model of sea ice growth. *Modeling the Earth System,* D. Ojima, Ed., UCAR/Office for Interdisciplinary Earth Studies, 225–238.

Walsh, J. E., and W. L. Chapman, 1990: Arctic contribution to upper-ocean variability in the North Atlantic *J. Climate,* **3,** 1462–1473.

Weaver, A. J., E. S. Sarachik, and J. Marotzke, 1991: Freshwater flux forcing of decadal and interdecadal oceanic variability. *Nature,* **353,** 836–838.

Welander, P., 1977: Thermal oscillations in a fluid heated from below and cooled to freezing from above. *Dyn. Atmos. Oceans,* **1,** 215–223.

——, 1986: Thermohaline effects in the ocean circulation and related simple models. *Large-Scale Transport Processes in Oceans and Atmosphere,* J. Willebrand and D. L. T. Anderson, Eds., D. Reidel, 163–200.

Willmott, A. J., and L. A. Mysak, 1989: A simple steady-state coupled ice–ocean model, with application to the Greenland–Norwegian Sea. *J. Phys. Oceanogr.,* **19,** 501–518.

Winton, M., and E. S. Sarachik, 1993: Thermohaline oscillation induced by strong steady state forcing of ocean general circulation models. *J. Phys. Oceanogr.,* **23,** 1389–1410.

Yang, J., and J. D. Neelin, 1993: Sea-ice interaction with the thermohaline circulation. *Geophys. Res. Lett.,* **20,** 217–220.

——, and S. Honjo, 1996: Modeling the near-freezing dichothermal layer of the Sea of Okhotsk. *J. Geophys. Res.,* **101** (C7), 16 421–16 433.

——, and R. X. Huang, 1996: The annual cycle and its role in generating interannual and decadal variations at high-latitude oceans. *Geophys. Res. Lett.,* **23,** 269–272.

——, and J. D. Neelin, 1996: Sea-ice interaction and the stability of the thermohaline circulation in response to long-term climate change. *Atmos.–Ocean,* in press.

Zhang, S., C. A. Lin, and R. J. Greatbatch, 1995: A decadal oscillation due to the coupling between an ocean circulation model and a thermodynamic sea-ice model. *J. Mar. Res.,* **53,** 79–106.